8-2020

Modeling the Obscuring Features in Active Galactic Nuclei: an X-Ray Analysis of NGC 1052

Samantha E. Cabral

University of Massachusetts Boston

Recommended Citation

Cabral, Samantha E., "Modeling the Obscuring Features in Active Galactic Nuclei: an X-Ray Analysis of NGC 1052" (2020). *Graduate Masters Theses*. 630.
https://scholarworks.umb.edu/masters_theses/630

MODELING THE OBSCURING FEATURES IN ACTIVE GALACTIC NUCLEI: AN X-RAY ANALYSIS OF NGC 1052

A Thesis Presented

by

SAMANTHA E. CABRAL

Submitted to the Office of Graduate Studies, University of Massachusetts
Boston, in partial fulfillment of the requirements for the degree of

MASTER OF SCIENCE

August 2020

Physics Program

MODELING THE OBSCURING FEATURES IN ACTIVE GALACTIC NUCLEI:

AN X-RAY ANALYSIS OF NGC 1052

A Thesis Presented

by

SAMANTHA E. CABRAL

Approved as to style and content by:

Stephen Arnason, Associate Professor
Chairperson of Committee

Jonathan Celli, Associate Professor
Member

Chandra Yelleswarapu, Associate Professor
Member

Mislav Baloković, Fellow
Black Hole Initiative, Harvard University
Member

Jonathan Celli, Program Director
Physics Program

Rahul Kulkarni, Chairperson
Physics Department

ABSTRACT

MODELING THE OBSCURING FEATURES IN ACTIVE GALACTIC NUCLEI: AN X-RAY ANALYSIS OF NGC 1052

August 2020

SAMANTHA E. CABRAL,
B.S., University of Massachusetts Amherst
M.S., University of Massachusetts Boston

Directed by Associate Professor Stephen Arnason

We present a multi-epoch analysis of the X-ray spectrum of NGC 1052, a nearby galaxy notorious for its well-studied spectral variability. We utilize observations from *NuSTAR*, *XMM-Newton*, *Chandra*, *Swift*, *Suzaku*, *BeppoSAX*, and *ASCA* to create a comprehensive set of data that spans roughly 20 years. Organizing our data by observation date and grouping into specific epochs allows us to explore a model allowed to flex and accommodate any spectral changes that occur over time in the X-ray spectrum of NGC 1052. We find that the spectrum takes on a relatively flat nature and is best modeled with two neutral absorption components in addition to a component representing torus reprocessing. We are able to successfully constrain properties of the dense obscuring torus, reporting a high covering factor of $\sim 80\%$.

TABLE OF CONTENTS

LIST OF TABLES

Table Page

LIST OF FIGURES

Figure Page

CHAPTER 1

INTRODUCTION

1.1 Active Galactic Nuclei

An extremely luminous compact region known as an active galactic nucleus (AGN) lives at the center of a small fraction of large galaxies. As the most consistently luminous sources in the observable universe, AGN luminosity is distributed across the electromagnetic spectrum with strong emissions observed in the X-ray and infrared bands. This strong radiative output is assumed to be powered by the accretion of material onto the supermassive black hole (SMBH) located at the AGN's center.

It is commonly suggested that material flowing inward to the SMBH takes on the configuration of a geometrically thin accretion disk [Shakura and Sunyaev, 1973]. Blackbody photons from the inner region of the accretion disk approach the corona, a neutral region surrounding the SMBH composed of hot gas and relativistic protons and electrons. The incident photons are Compton scattered by electrons in the corona, producing high-energy X-rays which we observe [Haardt and Maraschi, 1991]. This intrinsic spectrum is well approximated as a power law with an exponential cutoff at high energies. In addition to being observed directly, the powerlaw continuum is partially reprocessed while traveling through the outer regions of the accretion disk. While the accretion disk takes on the geometry of a thin disk, it is considered to be optically thick.

The simplest standard model for AGN suggests that there is a dense toroidal structure (commonly known as a torus) comprised of gas and dust located at the outer extremities of the AGN's accretion disk [Antonucci, 1993, Urry and Padovani, 1995]. As incident X-rays travel through the torus, they are subject to a significant amount of absorption and reprocessing. This reprocessed emission from the torus is primarily observed in the infrared portion of the spectrum. However, two distinct signatures of torus reprocessing emerge in the X-ray band: a narrow Fe Kα emission line with a rest-frame energy of 6.4 keV, and a Compton hump peaking at ~ 30 keV [George and Fabian, 1991].

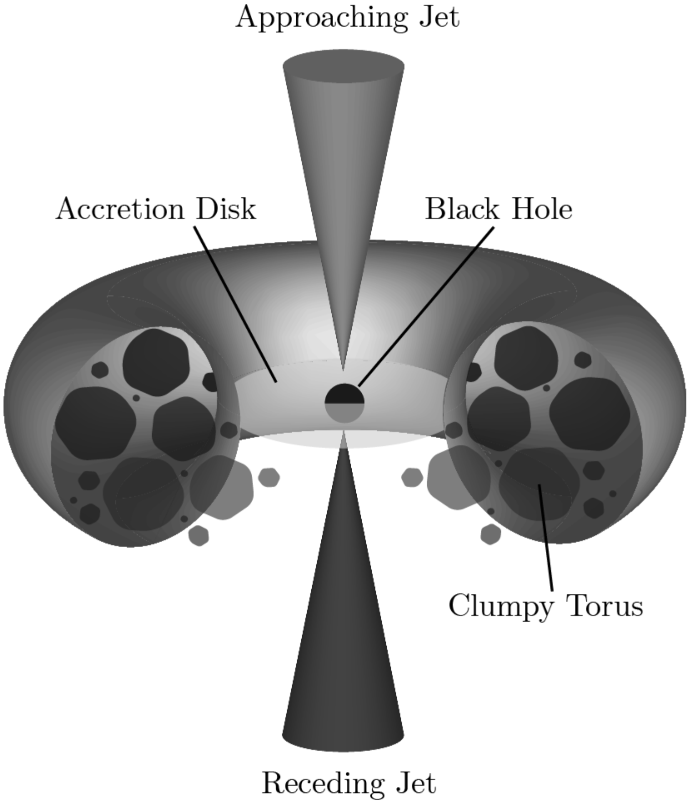

Figure 1: The current standard model for AGN. Material approaching the central SMBH takes on the form of a geometrically thin accretion disk. A dense torus surrounds the central region and is composed of thick, compact clouds. In radio-loud AGN, large-scale radio jets extend out on galactic scales.

Significant variation in X-ray absorption on the time scale of years, months, weeks, and even days has indicated that the obscuring torus most likely takes on an anisotropic, clumpy distribution where gas adopts the form of thick, compact clouds. As these clouds pass through the line of sight between the observer and the central engine, a more significant amount of obscuration will occur [Risaliti et al., 2002, Markowitz et al., 2014].

Strong magnetic fields can lead to the formation of relativistic jets that extend from the central region on megaparsec[1] scales, or the scale commonly used to quantify the diameter of galaxy clusters. By considering the orientation of relativistic jets and the obscuring torus, we can categorize AGN into two types of Seyfert galaxies, which in general describe spiral galaxies with bright nuclei. In Seyfert I galaxies, the AGN is oriented with the jet axis pointed towards an observer. In Seyfert II galaxies, the observer views the central engine "edge-on", or through the torus. In Figure 1, we illustrate the current standard model for AGN, demonstrating the geometry and relation to the AGN's central SMBH, the thin accretion disk, the dense obscuring torus, and the approaching and receding jets.

Spectral analysis of AGN emission in the X-ray band is crucial in understanding absorption characteristics of obscured AGN. By modeling the spectral features present due to reprocessing of the torus, we can constrain some of its properties and improve our understanding of the nature of obscured AGN [Krolik et al., 1994, Levenson et al., 2002].

1.2 NGC 1052

In this thesis, we explore a multi-epoch approach to analyze the NGC 1052 broadband X-ray spectrum. NGC 1052 is a relatively nearby elliptical galaxy housed within the Virgo Cluster at a distance of roughly 18 Mpc [Jensen et al., 2003]. It hosts a low-

---

[1] 1 parsec = 3.08×10^{16} meters, roughly 3.26 light years

luminosity AGN at its center along with a prominent double-sided jet oriented at a minimum inclination angle of 76° [Sawada-Satoh et al., 2008]. Its classification as a Seyfert II galaxy tells us that we view the central region edge-on, rather than along the jet axis.

NGC 1052 is a valuable source for studying AGN structure. Its relative proximity and brightness allow for a more detailed characterization of the central engine environment than what is typically attainable. The relatively high inclination angle suggests that the approaching jet does not have a significant contribution to the X-ray spectrum, and we can assume the majority of the X-ray emission characterizes the workings of the innermost regions of the AGN. NGC 1052 is well-documented in studies spanning a variety of energy ranges [Kameno et al., 2001, Kadler et al., 2004].

CHAPTER 2

DATA REDUCTION AND ANALYSIS

For our X-ray analysis of NGC 1052, we utilize observations from seven different space-based observatories. The observatories that make up our comprehensive list are *ASCA*, *BeppoSAX*, *Chandra*, *XMM-Newton*, *Swift*, *Suzaku*, and *NuSTAR*. Each X-ray observatory utilizes different software and methods for data reduction, which is described in detail in Chapter 2.

2.1 Astronomical X-ray Data Acquisition

While each X-ray observatory has different data reduction methods and instrument specifications, the overall instrumental design and general method of data acquisition has the same primary approach. The design of X-ray instruments is extremely different from that of optical instruments. Atmospheric absorption requires X-ray instruments to be placed in orbit outside the atmosphere, which differs from the ground-based approach allowed by instruments operating in the radio, infrared, and visible bands. Optical observations employ mirrors to focus incident light before traveling to a detector. However, X-rays are far too energetic and pass directly through the focusing mirrors, requiring X-ray instruments to have an entirely different geometry for diverting the incident photon paths.

To focus high-energy X-rays, mirrors with an orientation nearly parallel to the photon's beam are utilized. This evokes a grazing incidence, allowing the X-ray photons to converge towards a detector. The majority of X-ray telescopes utilize Charge-coupled Devices (CCDs) to translate focused incident photons from distant sources into readable images. Once the raw data are processed, these images can be displayed with software like DS9, a data visualization application designed by the Smithsonian Astrophysical Observatory (SAO). To correctly define the source spectrum from an image, the background region first needs to be specified from a source-free area. Once the source and background regions are correctly defined, analysis tools can be used to correctly remove the background spectra. An example of this process can be seen in Figure 2, where the source is defined as a circular region and the background is defined as a polygon for the FPMA image provided by *NuSTAR*'s February 2013 observation (OBSID 60061027002).

Furthermore, observations need to consider instrument response files to produce a final spectrum. These are files that contain crucial information regarding instrumental specifications, such as effective area of the detector and quantum efficiency as a function of photon energy. The typical approach for visualizing acquired data first explores the distribution of count rates within a range of binned energies. In Figure 3, we plot the count rate $n(E)$ as a function of energy on a log scale. The count rate holds the unit s^{-1}, which defines counts occurring per second, which is then divided by keV to normalize the width of energy bins across a large energy range when plotting on a logarithmic scale. This is typically referred to as the "folded" spectrum. We utilize a joint *NuSTAR* and *XMM-Newton* from 2017 January 17 as a sample observation to visualize the folded spectrum, though details on these observations will be further explained later in this chapter.

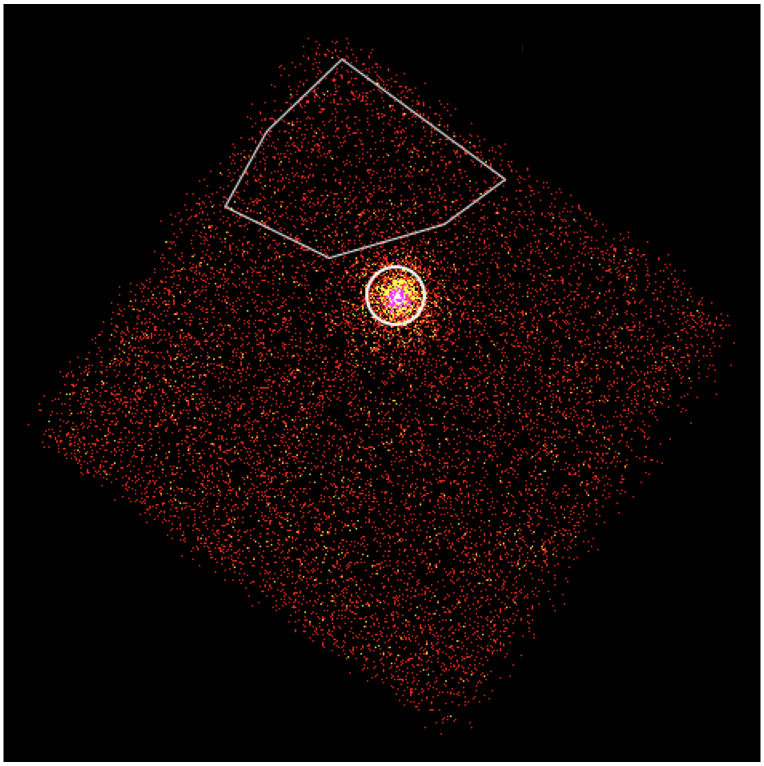

Figure 2: Defining source and background regions in X-ray observations. As a demonstration, the source and background regions are defined here in DS9 using circular and polygonal regions, respectively, for the *NuSTAR* observation provided by FPMA for OBSID 60061027002.

With the folded spectrum defined, we can now visualize what is typically referred to as the "unfolded" spectrum. The folded spectrum is first divided by the appropriate response file to correctly consider the effective collecting area of the instrument, which introduces a factor of cm^{-2}. A factor of keV^2 is then introduced by first multiplying the spectrum by the width of each bin, allowing us to translate counts per bin to a more useful quantity, photons per bin. The spectrum is then multiplied by the average energy per bin. In Figure 4, we visualize the unfolded spectrum, $E^2 n(E)$, when plotted as a function of energy on a logarithmic scale for the same spectra used in Figure 3. Important features emerge when plotting the unfolded spectrum. A distinct peak at 6.4 keV represents the narrow Fe Kα emission line, and a soft excess is apparent with a

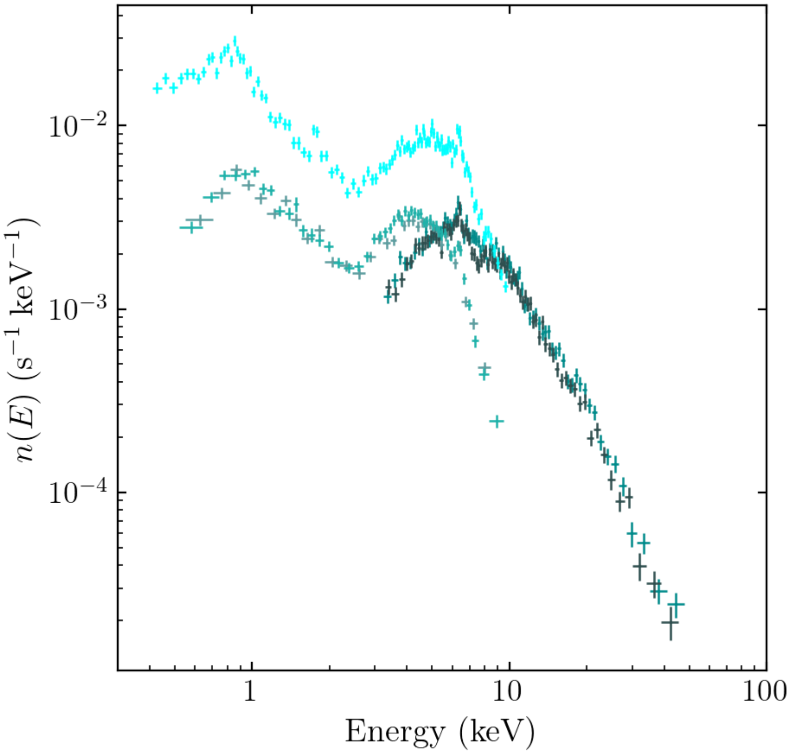

Figure 3: Visualizing the folded spectrum. For a sample observation, count rate as a function of energy is plotted on a logarithmic scale.

peak ~ 1 keV. For the remainder of this thesis, spectra will be plotted in terms of the unfolded spectrum.

2.2 *ASCA*

The Advanced Satellite for Cosmology and Astrophysics (*ASCA*) [Tanaka et al., 1994] was a Japanese X-ray observatory launched in February 1993 and served as a collaboration between U.S. and Japanese institutions. *ASCA* was monumental, being the first mission in X-ray astronomy to employ Charged- Coupled Devices (CCDs). The satellite

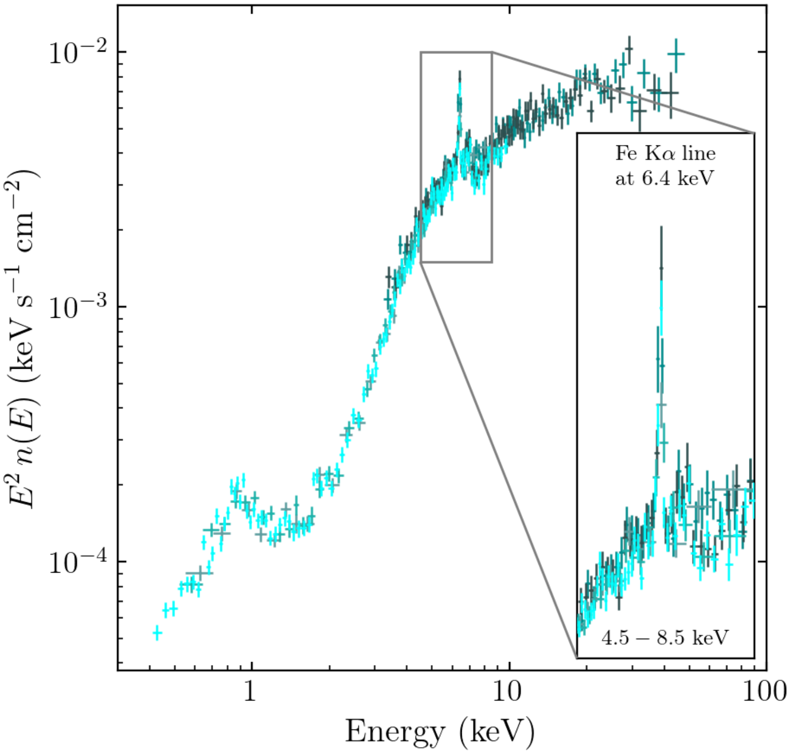

Figure 4: Visualizing the unfolded spectrum. The folded spectrum is divided by a response file, then multiplied by bin width and average photon energy per bin. The resulting plot shows distinct features, such as the Fe Kα emission line with a rest energy of 6.4 keV shown here as the inset.

carried four large imaging telescopes that focus X-rays onto two pairs of detectors located at the focal plane. Two of these telescopes are Solid-State Imaging Spectrometers (SIS, referred to as SIS0 and SIS1 in this paper) which operate in the 0.4-10 keV range [Inoue, 1993]. The remaining two are Gas Imaging Spectrometers (GIS, referred to as GIS2 and GIS3) which operate in the 0.7 to 10 keV range [Ohashi et al., 1996].

ASCA observed the source on 1996 August 11 (OBSID 74061000), which serves as the first observation of NGC 1052 in the 2-10 keV band. Processed spectral files and response files for all four instruments were downloaded from the *Tartarus Database*[1]. Exposure times vary for different instruments, but range between 35.7 ks and 38.6 ks.

2.3 *BeppoSAX*

BeppoSAX [Boella et al., 1997a] was a major X-ray mission for the Italian Space Agency and was launched in April 1996. The Narrow Field Instruments (NFI) on board are partly comprised of four X-ray telescopes. One of these telescopes is a Low Energy Concentrator Spectrometer (LECS) which operates in the 0.1-4 keV range [Parmar et al., 1997], while the remaining three are Medium Energy Concentrator Spectrometers (MECS) which operate in the 1.3-10 keV range [Boella et al., 1997b]. However, during the time of observation, only two of the MECS detectors were operational. The NFI also houses the Phoswich Detection System (PDS), which operates in the 15-300 keV range [Frontera et al., 1997] to help extend the observational capabilities of *BeppoSAX* to consider hard X-rays.

Processed data were downloaded from NASA's High Energy Astrophysics Science Archive Research Center (HEASARC) and contained spectra from LECS and MECS. Data reduction and analysis followed standard procedures as outlined in the ***BeppoSAX* ABC Guide**[2]. *BeppoSAX* observed the source on 2000 January 11 (OBSID 5082800). Source spectra were extracted from circular regions with 180" radii centered on the source. The spectra produced by MECS 2 and 3, the two operational MECS detectors, were co-added. The appropriate response and background files were downloaded from the online repository[3] maintained by the Italian Space Agency (ASI). The exposure times for LECS, MECS, and PDS are 25.7, 47.5, and 30.0 ks, respectively.

---

[1] `https://heasarc.gsfc.nasa.gov/FTP/asca/data/tartarus/`

[2] `https://heasarc.gsfc.nasa.gov/docs/sax/abc/saxabc/saxabc.html`

[3] `ftp://ftp.asdc.asi.it/sax/cal`

2.4 *Chandra*

The *Chandra* X-ray Observatory [Weisskopf et al., 2002] launched in July 1999 and served as the X-ray addition to NASA's Great Observatories program. *Chandra* utilizes two main instruments, a High Resolution Camera (HRC) and an Advanced CCD Imaging Spectrometer (ACIS) to provide sensitive coverage in the 0.1-10 keV range.

The standard reduction and analysis steps are detailed in the **Ciao Analysis Guides**[4] provided by the Chandra X-ray Center. Data from *Chandra* were obtained from HEASARC and all featured observations collected by the ACIS instrument, and observations from *Chandra* were processed using CIAO v4.11

Chandra observed the source on 2005 September 18 (OBSID 5910) for a duration of 2.3 ks and 2001 September 5 (OBSID 385) for 59.2 ks. For each of the two observations, source extraction regions were specified in DS9 using a circular region with a radius of 15.9" centered on the NGC 1052 nucleus. The background region was specified in a source-free area, similar to data extraction for other observatories as specified in this paper. Once these regions were specified, `specextract` was used to generate spectra and response matrices.

2.5 *XMM-Newton*

The *XMM-Newton* observatory [Jansen et al., 2001] was launched by the European Space Agency (ESA) in December 1999 as part of their Horizon 2000 program. The European Photon Imaging Camera (EPIC) on board *XMM-Newton* is composed of three CCD cameras, each housed on a separate X-ray telescope. Two of these cameras are Metal Oxide Semi-conductor CCD arrays (commonly known as MOS; referred to as MOS1

---

[4] `http://cxc.harvard.edu/ciao/guides/acis_data.html`

and MOS2) which only consider a portion or the original incoming flux. The third camera views an unobstructed incident beam and uses pn CCDs (commonly known as pn). Together, the three cameras cover an energy range of 0.15-15 keV.

The Observation Files (ODFs) were obtained from the *XMM-Newton* Science Archive. Standard procedures for data reduction and analysis were followed as outlined in the **XMM-Newton ABC Guide**[5]. Data were processed using *XMM-Newton* Science Analysis System (SAS) v17.0 [Gabriel et al., 2004].

XMM-Newton observed the source on 2017 January 1 (OBSID 0790980101) for a duration of CHECK ks, 2009 August 12 (OBSID 0553300401) for a duration of CHECK ks, and 2006 January 12 (OBSID 0306230101) for a duration of CHECK ks. Source data were extracted using circular regions of 67.5” and 72.2” for MOS1 and MOS2 respectively, and 68.4” for pn. Background regions were again extracted from image regions with low photon activity. Once these regions were specified, response files were generated for each detector using `rmfgen` and `arfgen`.

2.6 *Swift*

The *Swift* Observatory was launched by NASA in November 2004. *Swift* is comprised of three co-aligned instruments, The Burst Alert Telescope (BAT), X-ray Telescope (XRT), and Ultraviolet/Optical Telescope (UVOT), that work together to form a powerful multiwavelength observatory.

---

[5] `https://heasarc.gsfc.nasa.gov/docs/xmm/abc/`

2.6.1 *Swift*/BAT

Swift/BAT [Krimm et al., 2013] is the largest of the instruments of the *Swift* observatory and operates in the 14-195 keV range. In addition to its ability to detect Gamma Ray bursts, BAT can run in a survey mode, performing an all-sky X-ray survey to provide a long-term average hard X-ray spectra for bright, local AGN. The first 105 months of observations made by *Swift*/BAT have been made public as an online catalogue[6] of X-ray sources detected by the instrument. We utilize the NGC 1052 source data from the *Swift*/BAT catalogue to serve as a time-averaged spectrum. While the downloaded spectra are ready for analysis, the data processing procedures are publicly available [Oh et al., 2018].

2.6.2 *Swift*/XRT

Swift/XRT [Gehrels and Swift Team, 2003] was designed to measure the simultaneous X-ray spectra of Gamma Ray Bursts detected by *Swift*/BAT and operates in the 0.2-10 keV range. Data were downloaded and processed through the online interface provided by the ASI Space Science Data Center[7].

The source was observed by *Swift*/XRT 2015 January 19 (OBSID 00030874001) for 9.4 ks, 2009 June 29 (OBSID 00030874016) for 3.7 ks, 2009 June 26 (OBSID 00030874014) for 9.8 ks, 2008 September 12 (OBSID 00030874007) for 3.9 ks, 2008 September 9 (OBSID 00030874006) for 4.8 ks, and 2007 August 4 (OBSID 00030874003) for 2.4 ks. *Swift*/XRT data when loaded as individual epochs did not provide photon statistics comparable to other instruments. Thus, in Section 3.2, XRT exposures are

---

[6] `https://swift.gsfc.nasa.gov/results/bs105mon/`

[7] `http://www.asdc.asi.it/mmia/index.php?mission=swiftmastr`

coadded and their response files are combined using a custom script based on standard `ftools`.

2.7 *Suzaku*

Suzaku [Mitsuda et al., 2007] was a Japanese X-ray observatory launched in July 2005 and, like *ASCA*, served as a collaboration between U.S. and Japanese institutions. *Suzaku* is comprised of two co-aligned instruments, a X-ray Imaging Spectrometer (XIS) operating in the 0.2-10 keV range [Koyama et al., 2007], and a collimated Hard X-ray Detector (HXD) operating in the 10-600 keV range [Takahashi et al., 2007]. At launch, the XIS consisted of four imaging CCD cameras (nicknamed XIS0-4). However, in November 2006, the majority of the imaging area of XIS2 became unusable. Therefore, we employ observations from the HXD (referred to as PIN) in addition to observations provided by XIS0, XIS1, and XIS3.

The data were downloaded via HEASARC and reduced using the standard procedures as outlined in the **Suzaku ABC Guide**[8]. *Suzaku* observed the source on 2007 February 16 (OBSID 702058010). Once filtered, the exposure times were 83.5 ks for the three XIS detectors and 78.1 ks for the HXD/PIN detector. XIS source extraction regions were specified in DS9 using circular regions with a radius of 180" centered on the source. The background region was specified using source-free circular areas for each XIS detector.

Once these regions were specified, the tasks `xisrmfgen` and `xissimarfgen` were utilized to generate response matrices for each XIS detector. The spectra from XIS0 and XIS3 were coadded (referenced as XIS0+3 throughout this paper). These spectra were binned with a minimum of (blank) counts per bin, and data outside of the 0.5-8.5

---

[8] https://heasarc.gsfc.nasa.gov/docs/suzaku/analysis/ abc/

keV range were ignored. For HXD/PIN, the `hxdpinxbpi` script was used to generate response files and background spectrum. The PIN spectrum is background-dominated, so we grouped the data with a minimum of 3000 counts per bin. This resulted in 12 bins over an energy range of 12-70 keV.

2.8 *NuSTAR*

The *Nuclear Spectroscopic Telescope Array* (*NuSTAR*) [Harrison et al., 2013] was launched in June 2012 and became the dominant observatory for hard X-ray observations, operating in the 3-79 keV band. *NuSTAR* is comprised of of two co-aligned X-ray telescopes, FPMA and FPMB, that observe a source simultaneously while carried by a three-axis-stabilized spacecraft. The two telescopes each features a focal plane of pixel detectors arranged in a 2x2 grid.

Typical data reduction and analysis steps as outlined in the **NuSTAR Data Analysis Software Guide**[9] were followed. We employed the standard *NuSTAR* data analysis software, NuSTARDAS v1.8.0, provided within HEASOFT v6.26 along with the *NuSTAR* calibration database, CALDB v20190430. Upon downloading *NuSTAR* data from HEASARC, observations are not ready for analysis and need to first be sent through `nupipeline`, a script that takes the downloaded data in FITS format and produces clean, calibrated event files. This is accomplished by applying pre-specified cleaning criteria based on *NuSTAR* instrument parameters and event properties. The result is event files that are ready for analysis in DS9,

NuSTAR observed the source on 2013 February 14 for a total time of 15.6 ks (OBSID 60061027002) and 2017 January 1 (OBSID 60201056002) for a total time of 59.8 ks. Source spectra are extracted using circular regions in DS9 centered on NGC 1052. A

---

[9] `https://heasarc.gsfc.nasa.gov/docs/nustar/analysis/nustar_swguide.pdf`

circular region with radius of 47.4” was utilized for OBSID 60061027002 along with a radius of 87.3” for OBSID 60201056002. Background regions were then specified with a polygon in a source-free region that is housed within the same chip as the source. Once regions are specified, the `nuproducts` task is used to generate source and background spectra.

2.9 Observation Summary

By utilizing observations from seven observatories, we observe NGC 1052 in an energy range spanning roughly 0.4 - 100 keV. This allows us to observe the AGN in both the soft ($<$ 10 keV) and hard ($>$ 10 keV) bands. In Table 1, we compile a detailed list of each individual observation used, characterized by OBSID, corresponding observatory, start date, and exposure time.

Table 1: Observational details for each epoch. Observations are listed in reverse chronological order, where Epoch 1 represents the most recent observation. Epoch 0 denotes the time-averaged *Swift*/BAT epoch.

Observatory	OBSID or SID	Start Date	Epoch	Exposure (ks)	Instrument(s)
Swift	105-month survey	-	0	1.855E4	BAT
NuSTAR	60201056002	2017 Jan. 17	1	47.03 48.57	FPMA FPMB
XMM-Newton	0790980101	2017 Jan. 17	1	49.42 68.23 43.17	MOS1 MOS2 pn
NuSTAR	60061027002	2013 Feb. 14	2	13.39 13.26	FPMA FPMB
XMM-Newton	0553300401	2009 Aug. 12	3	36.98 57.85 17.96	MOS1 MOS2 pn
Suzaku	702058010	2007 Feb. 16	4	78.09 100.7 201.3	XIS0+3 XIS1 PIN
XMM-Newton	0306230101	2006 Jan. 12	5	33.17 26.89	MOS1 pn
Chandra	5910	2005 Sep. 18	6	59.20	ACIS
BeppoSAX	50828001	2000 Jan. 11	7	25.73 63.69 30.03	LECS MECS2+3 PDS
ASCA	74061000	1996 Aug. 11	8	36.59 35.75 38.59 38.59	SIS0 SIS1 GIS2 GIS3

CHAPTER 3

METHODS AND MODELING

3.1 Single-Epoch Approach

We first explore creating a model using data from our most dominant epoch in terms of data quality. This allows us to explore features of the X-ray spectrum of NGC 1052 to create a comprehensive model which can later be applied to a collection of data spanning a broader set of dates. The combined 2017 *NuSTAR* and *XMM-Newton* observations creates an epoch that provides sensitive coverage in both the soft and hard X-ray bands, suggesting it should be used as the singular epoch when building our model.

3.1.1 The Intrinsic Spectrum

The intrinsic X-ray spectrum of AGN can be approximated as a power law with a gradual rolloff in the 300 keV range. We model this with the Xspec model `cutoffpl`, which is defined in Equation 3.1. In this equation, Γ represents the power law photon index, where a smaller value denotes a harder, flatter spectrum. The energy of the exponential rolloff is defined by β which we fix at 300 keV, and K denotes the normalization.

$$A(E) = KE^{-\Gamma}\exp(-E/\beta) \tag{3.1}$$

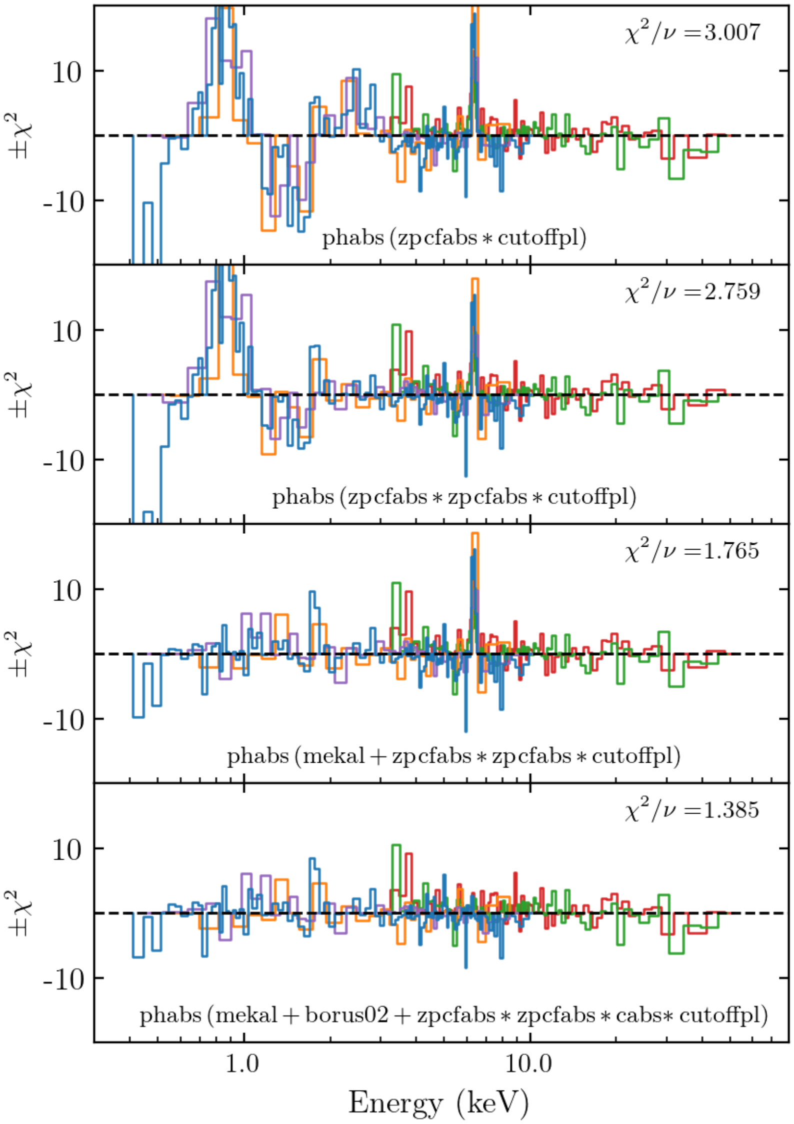

Figure 5: Residual comparison for single-epoch model variations. When building the single-epoch model, we utilize data from our most comprehensive epoch before applying our model to multi-epoch data. Each panel represents a significant change to the base model, justified both by the reduced chi-squared values and a visualization of improvement on residuals when fitting the corresponding model to the single-epoch data.

We need to consider that our source is located in a separate host galaxy, which will contribute photoelectric absorption to partly conceal the spectrum. We therefore scale the intrinsic spectrum with the Xspec model `phabs` which is defined by Equation 3.2. In this model, N_H represents the equivalent hydrogen column density (with units 10^{22} atoms cm^{-2}) and $\sigma(E)$ defines the photo-electric cross-section. We fix the line-of-sight column density at $N_{\mathrm{H}} = 2.83 \times 10^{22} \mathrm{cm}^{-2}$ [HI4PI Collaboration et al., 2016], which defines the expected additional absorption for NGC 1052 due to any galactic extinction.

$$M(E) = \exp[-N_H \sigma(E)] \tag{3.2}$$

Throughout the modeling process, we consider a reduced chi-squared statistic (χ^2/ν) to justify the reliability of our models, where ν represents the number of degrees of freedom. Considering the modeling components `cutoffpl` and `phabs` produces a starting fit statistic of $\chi^2/\nu = 12011.62/354$.

3.1.2 Absorption Components

Previous work has found that the X-ray spectrum of NGC 1052 shows significant absorption toward the nuclear emission region. It is believed that the main contributor to this absorption is the torus. As X-ray photons travel through the dense torus, they are subject to both photoelectric absorption and Compton scattering. To model the neutral absorption of the intrinsic spectrum, we use the Xspec model `zpcfabs` to modify the original power law component. The `zpcfabs` component is defined by Equation 3.3, and is similar to the form of Equation 3.2. Here, N_H again represents the equivalent line-of-sight absorption and $\sigma(E)$ defines the photo-electric cross-section. The newly introduced variables are z, the galactic redshift, and f, the dimensionless covering fraction which is reported as a value between 0 and 1. The covering fraction represents the amount of the incident spectrum that is absorbed.

$$M(E) = f \exp[-N_H \sigma(E[1+z])] + 1 - f \tag{3.3}$$

When considering this neutral absorption component within the model, the fit statistic is reduced to $\chi^2/\nu = 1058.48/352$ (3.007). However, residuals still remain at intermediate energies (1-4 keV). This is visualized within the first panel of Figure 5, which displays the residuals present when models are fit to single-epoch data. We therefore consider a second `zpcfabs` component to model these residuals, which produces an updated fit statistic of $\chi^2/\nu = 965.49/350$ (2.759). The residuals corresponding to the updated version of our model are displayed within the second panel of Figure 5.

3.1.3 Extended Emission Spectrum

Residuals further show a need for a soft component strongly peaking around 1 keV. Following previous analysis of the X-ray spectrum of NGC 1052 [Brenneman et al., 2009] we explore any additional extended emission contributions in our spectrum by including an additive `mekal` [Mewe et al., 1985] component. The `mekal` component accounts for any additional emission that may result from the host galaxy. This component allows us to define the plasma temperature, kT, in keV.

With the inclusion of a `mekal` component, we observe a drastic decrease in residuals present $<$ 1 keV range, which is visualized in the third panel of Figure 5. This produces an improved fit statistic of $\chi^2/\nu = 614.18/348$ (1.765).

3.1.4 Torus Reprocessing

Our model correctly accounts for line-of-sight absorption of the intrinsic X-ray spectrum with two `zpcfabs` components. However, it does not yet consider the reprocessing component present from the torus. We include `borus02` [Baloković et al., 2018] as an additive component to the original power law continuum, which allows any reprocessed emission to be incorporated into the model. The `borus02` component allows us to define the spectrum in terms of the AGN's inclination angle and torus covering factor. The torus is typically assumed to be a structure with dense, anisotropic nature. However, complexities arise when modeling such a dynamic feature. For simplicity, `borus02` models the torus as a uniformly dense sphere with conical cutouts along the jet axis.

While other methods for modeling torus reprocessing are used in other works, namely `MYtorus` [Murphy and Yaqoob, 2009] and `BNtorus` [Brightman and Nandra, 2011], we opt to use `borus02` for its inclusion of additional free parameters. Allowing variation in crucial parameters such as the iron abundance and high energy cutoff allow `borus02` to be applied to wider sample of AGN. This component considers the cosine of the inclination angle, which we define to be $cos(\theta_i) = 0.1736$ for an inclination angle of 80° above the line of sight.

It is important to note that `borus02` only considers scattering into the line of sight, but does not include photons Compton scattered out of the line of sight. To incorporate any possible extinction along the line of sight, we include the Xspec model `cabs` as a multiplicative component to our powerlaw. The `cabs` model is defined in Equation 3.4. This is similar to the equation for `phabs` seen in Equation 3.2. However, $\sigma_T(E)$ represents the Thomson cross-section with corrections at high energies. We consider the total column density for photons scattered out of the line of sight equal to the photons scattered in. We therefore set the `cabs` column density, N_{H}, to be equal to the sum of the equivalent parameter from both neutral absorption components.

$$M(E) = \exp[-N_H \sigma_T(E)] \tag{3.4}$$

With the inclusion of components modeling torus reprocessing and beam extinction, the fit statistic is slightly reduced to $\chi^2/\nu = 479.17/346$ (1.385). Residuals are improved upon in the 5-10 keV range, which is visualized in the bottom panel of Figure 5. The finalized single-epoch model takes on the following form in Xspec:

`phabs(mekal +atableborus02 + zpcfabs * zpcfabs * cabs * cutoffpl)`

3.2 Multi-Epoch Approach

As the model is now defined in the single-epoch setting, we can adapt our model for multi-epoch application. Our goal is to create an environment that will allow us to observe any possible spectral variability of NGC 1052 over the course of our 20-year span of observations. We accomplish this by allowing specific parameters unique values for each epoch. This differs from the default approach when applying a model to a large amount of spectra, which only considers the leading spectrum when fitting parameters. By freeing important parameters once per epoch, our model is allowed to vary and accommodate spectral changes present in each distinct epoch. When we apply the model defined in Section 3.1.4, the resulting fit statistic is $\chi^2/\nu = 5649.24/1793$ (3.15).

We first consider the multiple observatories that were utilized to acquire data. We account for a possible variation in instrumental flux calibration by including the Xspec model `constant`, which considers an energy-independent multiplicative factor. *NuSTAR* has the most overlap in energy with the long-exposure BAT observation and we consequently consider it to be perfectly calibrated. This requires both FPMA and BAT to hold cross-normalization constants of 1.0. Cross-normalization constants for *Swift*/XRT, *XMM-Newton*, and *Suzaku* are provided in previous literature [Madsen et al., 2017] with relation to a perfectly calibrated FPMA. However, the remainder of the cross-normalization constants require deriving. Values for *Chandra* and *ASCA* instruments are provided [Snowden, 2002] with relation to a perfectly calibrated SIS1. Instruments and corresponding cross-normalization constants can be seen in Table 2. Consideration for flux calibration produces a fit statistic of $\chi^2/\nu = 4044.82/1779$ (2.27).

Residuals are most significant in the high-energy range of each epoch. To address this, we designate each epoch a unique power law normalization by freeing the parameter. This allows the model to flex and accommodate changes in the high-energy range of each epoch's spectra. We designate a principal instrument for epochs that contain observations from multiple instruments, which will each hold a free, untied value corresponding to the powerlaw normalization parameter. We define these principal instruments to be *NuSTAR*/FPMA, *XMM-Newton*/MOS1, *Suzaku*/XIS1, *ASCA*/SIS0, and *BeppoSAX*/LECS. The normalization for the remaining instruments is then linked to the free normalization parameter defined by the principal instrument in their respective epoch. This same method will follow for other parameter variations throughout this thesis. *Swift*/BAT serves as a time-averaged spectrum of the eight unique epochs. Thus, it should hold a powerlaw normalization constant that is a numerical average of the eight freed normalization parameters present in the model. This produces an improved fit statistic of $\chi^2/\nu = 2284.17/1771$ (1.29).

We next explore if allowing each epoch a unique value for the neutral absorption column density yields a better fit of our data, which will allow us to explore how this parameter varies over time. Our model contains two neutral absorption modeling components

Table 2: List of instrumental cross-normalization constants. In each epoch, one instrument is considered perfectly calibrated, denoted here with a value of 1.0.

Observatory	**Instrument**	**Value**	**Reference**[a]
NuSTAR	FPMA	1.0	—
NuSTAR	FPMB	free	—
Swift	BAT	1.0	—
Swift	XRT	1.045	M17
XMM-Newton	MOS1	1.02[b]	M17
XMM-Newton	MOS2	free	—
XMM-Newton	pn	free	—
Suzaku	XIS0+3	0.94	M17
Suzaku	XIS1	free	—
Suzaku	PIN	1.12	M17
Chandra	ACIS	0.943	M17
ASCA	SIS0	1.047	S02+M17
ASCA	SIS1	free	—
ASCA	GIS2	free	—
ASCA	GIS3	free	—
BeppoSAX	LECS	1.0	F99
BeppoSAX	MECS2+3	free	—
BeppoSAX	PDS	1.15	F99

Notes: [a] References: M17=[Madsen et al., 2017], S02=[Snowden, 2002], F99=Fiore et al. (1999), Cookbook for *BeppoSAX* NFI Spectral Analysis; [b] Free in the epoch shared with *NuSTAR*.

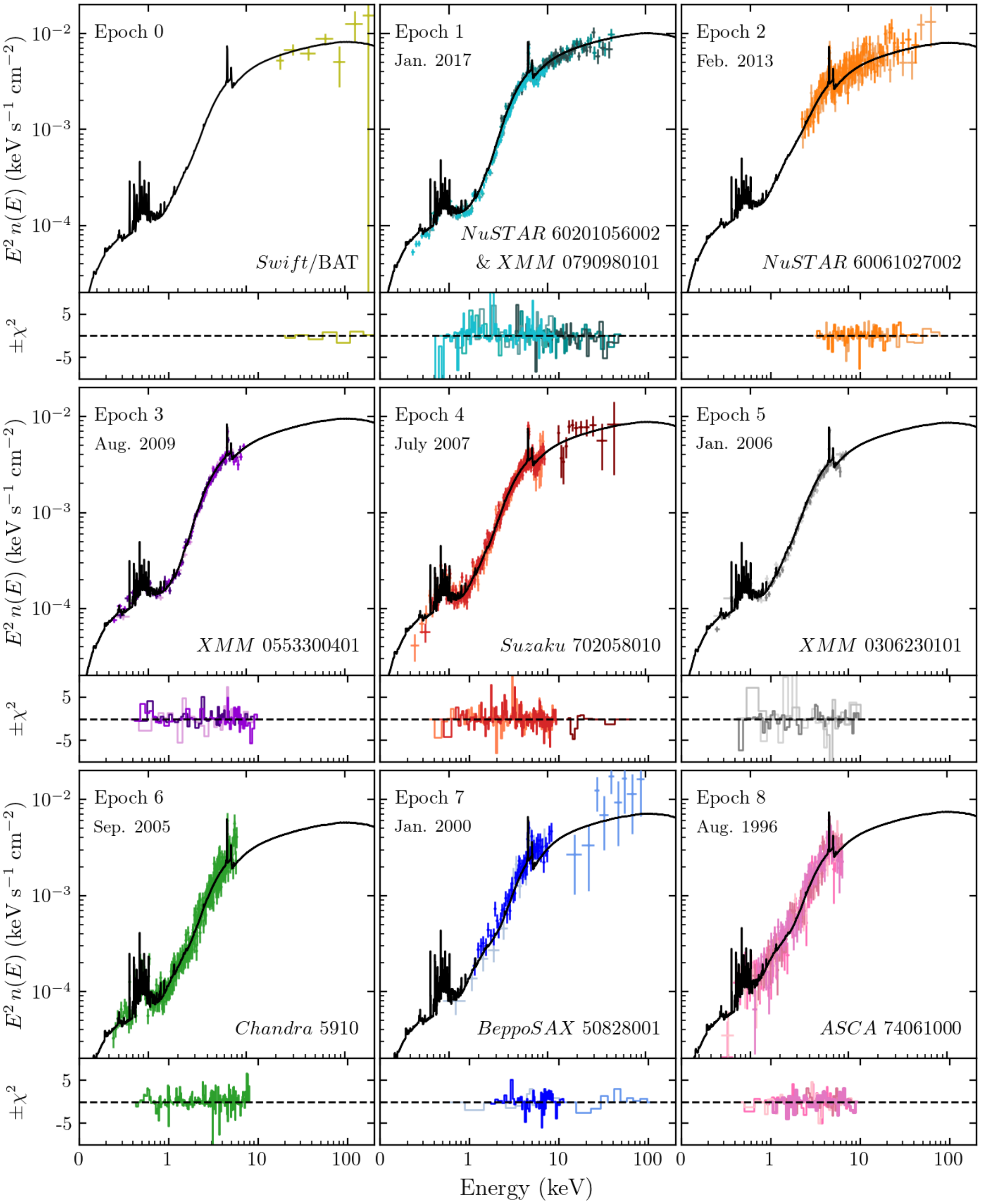

Figure 6: Multi-epoch model comparison. Data is plotted for each of the individual eight epochs in addition to the time-averaged epoch. Data is organized by observation date from most recent observation (Epoch 1) to oldest observation (Epoch 8). Below each epoch is a residual plot, showing which energy bins contribute most to the fit's chi-squared value.

(`zpcfabs`), which requires us to test different combinations of parameter variation. We test three different situations:

1. only the line-of-sight column density from the first neutral absorption component ($N_{\mathrm{H},1}$) varies, producing a fit statistic of $\chi^2/\nu = 2062.39/1765$ (1.17),
2. only the line-of-signt column density from the second neutral absorption component ($N_{\mathrm{H},2}$) varies, producing a fit statistic of $\chi^2/\nu = 2100.07/1764$ (1.19), and
3. both neutral column densities ($N_{\mathrm{H},1}$ + $N_{\mathrm{H},2}$) vary together, producing a fit statistic of $\chi^2/\nu = 1910.13/1760$ (1.085).

The third variation of this step results in the best fit, and we proceed forward with each epoch holding a freed value for line-of-sight column densities of both neutral absorption components simultaneously. This current model will be referred to as “Model 1” for later comparison with other well-fitting models.

We need to again consider that the *Swift*/BAT spectrum is a time-averaged observation. To reflect this in our model, we set the values of both $N_{\mathrm{H},1}$ and $N_{\mathrm{H},2}$ for the *Swift*/BAT epoch equal to the numerical average of the untied column densities from the remaining eight epochs. However, an issue arises with Epoch 2 containing the lone *NuSTAR* observation. A lack of data coverage in the low-energy band leads to an untied $N_{\mathrm{H},1}$ that cannot be constrained well. Therefore, this parameter is excluded from the *Swift*/BAT average, and within Epoch 2 the column density is set to equal this average for simplicity. This issue was not present when constraining $N_{\mathrm{H},2}$ within Epoch 2 due to data coverage in the energy range where the second `zphabs` component most effects the model.

Our model currently features variations in line-of-sight column density from both neutral absorbers, $N_{\mathrm{H},1}$ and $N_{\mathrm{H},2}$. In Section 3.1.4, we define the `cabs` column den-

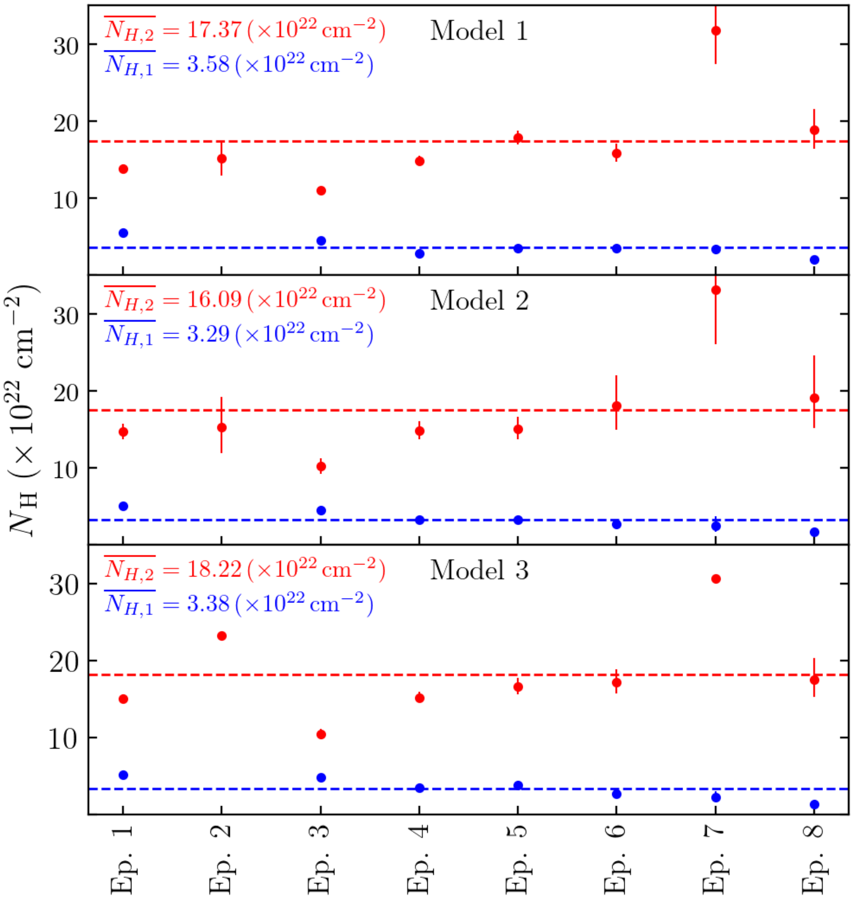

Figure 7: Time variation in the line-of-sight column density. For each of the three best-fitting models, N_H values are quantified for each neutral absorption modeling component. Each of the unique eight epochs are represented, and dashed lines represent the averaged value held by the *Swift*/BAT epoch. In Epoch 2, $N_{\mathrm{H},1}$ cannot be well-constrained as a free parameter due to a lack of low-energy coverage where the first neutral absorption component dominates within the model. It is therefore not represented within this figure, and set equal to the *Swift*/BAT average within the model.

sity ($N_{\rm H,Comp}$) to be equal to the sum of the column densities from the two absorption components. In the multi-epoch setting, this model component will now need to reflect the newly allotted variation in column density. We accomplish this by setting $N_{\rm H,Comp}$ equal to the sum of $N_{\rm H,1}$ and $N_{\rm H,2}$ in each epoch. For the *Swift*/BAT epoch, we again set the value for this parameter to be equal to the average of the varying $N_{\rm H,Comp}$ from the eight unique epochs. We then assume that the majority of molecular absorption in the NGC 1052 spectrum is due to the presence of the torus and set the torus column density ($\log N_{\rm H,tor}$) equal to the line-of-sight column density ($\log N_{\rm H,Comp}$). In the single-epoch setting, this parameter within the `borus02` model remained an untied parameter. These updates to the model produce a fit statistic of $\chi^2/\nu = 1908.16/1759$ (1.08).

We now aim to explore possible variation in the structure of the absorber over time, parameterized by the line-of-sight covering factor. Similar to the strategy used when exploring variation in line-of-sight column density, we test two different situations:

1. only the covering fraction from the first neutral absorber (C_1) varies, producing a fit statistic of $\chi^2/\nu = 1884.42/1754$ (1.074), and
2. only the covering fraction from the second neutral absorber (C_2) varies, producing a fit statistic of $\chi^2/\nu = 1881.47/1753$ (1.073).

Throughout the paper, these models will be referred to as "Model 2" and "Model 3", respectively. Model 3 produces a slightly better fit in comparison, and our finalized model only includes variations in C_2. Again, in both Model 2 and Model 3, the *Swift*/BAT covering fractions were considered to be an average of the free covering fractions from the eight unique epochs. However, issues arise when considering C_1 within Model 2. This model features variation in $N_{\rm H,1}$, which previously could not be constrained when left as a free parameter in Epoch 2. Consequently, the same issue arises when considering the covering fraction, and the covering fraction corresponding to $N_{\rm H,1}$ can not be left free.

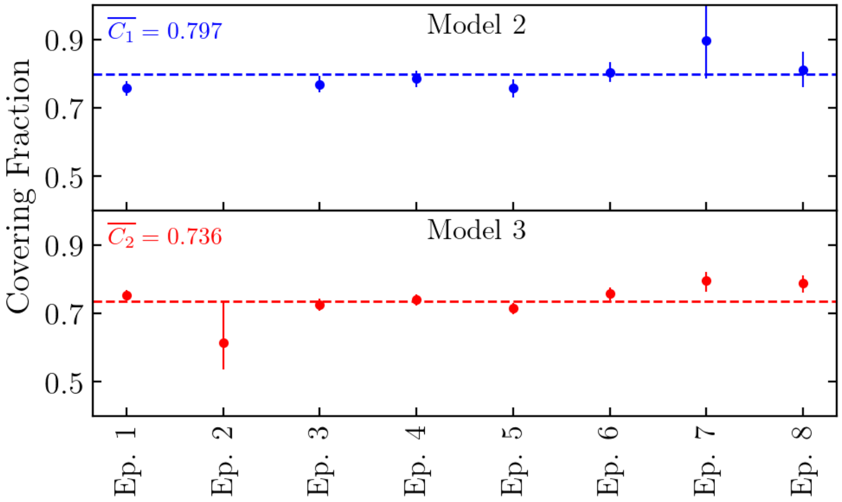

Figure 8: Time variation in the covering fraction. Similar to the structure of Figure 7, C_1 and C_2 are quantified for the corresponding neutral absorption modeling component as reported in Model 2 and Model 3. In Epoch 2, $N_{H,1}$ could not be left as a free parameter due to lack of low-energy coverage within that epoch. Similarly, C_1 can also not be well-constrained, and is omitted from the plot.

In Figure 7, we visualize the variation over time present in the parameters $N_{H,1}$ and $N_{H,2}$ in Model 1, Model 2, and Model 3. As previously mentioned, the first neutral column density could not be well-constrained when left as a free parameter in Epoch 2. Therefore, it is not shown in this plot, and within the model the value is set equal to the *Swift*/BAT average. The variation over time for the covering fractions for Model 2 and Model 3 is visualized in Figure 8, where again the value for C_1 in Epoch 2 cannot be left as a free parameter.

CHAPTER 4

DISCUSSION

4.1 The X-ray Spectrum of NGC 1052

Our modeling process and spectral analysis allows us to better constrain the geometry of the central engine environment in NGC 1052. We find that the line-of-sight column density varies between epochs, and likely consists of a neutral material that is best modeled with two neutral absorption components. In Figure 7, we visually compare the variations over time in column density present in all three of our best-fitting models. As the *Swift*/BAT epoch for each model has a column density defined to be the average of the free column densities from the remaining eight epochs, we can easily define an average line-of-sight column density for each of the two neutral absorbers. Our best-fitting model (Model 3) produces average column densities of $\overline{N_{\mathrm{H},1}} = 3.38 \times 10^{22}$ cm^{-2} and $\overline{N_{\mathrm{H},2}} = 18.07 \times 10^{22}$ cm^{-2}.

The variation in order of magnitude between the column densities of the two neutral absorbers is telling. It suggests that the second, more dominant absorber likely characterizes the presence of the obscuring torus, while the first, more subsidiary absorber suggests possible absorption from the AGN's host galaxy. This is justified by the lack of significant change over time for $N_{\mathrm{H},1}$ as seen in Figure 7. As dense clouds come in and out of the line-of-sight, the column density representing the presence of the dense torus should undergo significant fluctuations as we see with $N_{\mathrm{H},2}$. We observe a significant

Table 3: Free parameters and 1σ errors of best-fitting models. Below the parameters that are being quantified, the fit statistic of each model is represented, where the best-fitting model is Model 3.

Model Component	Parameter	Model 1	Model 2	Model 3
`mekal`	kT (keV)	$0.63^{+0.0094}_{-0.0095}$	$0.63^{+0.015}_{-0.016}$	$0.63^{+0.0094}_{-0.0095}$
	norm ($\times 10^{-5}$)	$2.82^{+0.097}_{-0.096}$	$2.82^{+0.016}_{-0.016}$	$2.81^{+0.098}_{-0.096}$
`borus02`	Γ	$1.65^{+0.014}_{-0.015}$	$1.66^{+0.015}_{-0.015}$	$1.66^{+0.015}_{-0.015}$
	$\log N_{\mathrm{H,tor}}$	23.32	23.32	23.33
	C_{tor}	$0.80^{+0.053}_{-0.045}$	$0.81^{+0.053}_{-0.050}$	$0.80^{+0.055}_{-0.053}$
`zpcfabs`	$\overline{N_{\mathrm{H}}}$ ($\times 10^{22}$ cm^{-2})	3.59	3.29	3.38
	Covering Fraction	$0.79^{+0.010}_{-0.012}$	0.80^{+}_{-}	$0.80^{+0.011}_{-0.012}$
`zpcfabs`	$\overline{N_{\mathrm{H}}}$ ($\times 10^{22}$ cm^{-2})	17.36	17.54	18.07
	Covering Fraction	$0.74^{+0.013}_{-0.014}$	$0.76^{+0.020}_{-0.022}$	0.74
	χ^2/ν	1999.76/1841 (1.086)	1972.88/1835 (1.075)	1968.76/1834 (1.073)

increase in both $N_{\mathrm{H},2}$ and C_2 in Epoch 7 corresponding to 2000 January 11 *BeppoSAX* observation date, suggesting that a cloud within the torus may have been passing through the observational line-of-sight at that time.

In Figure 6 we visually compare the eight unique epochs, in addition to the time-averaged epoch, and corresponding model for each in reverse chronological order. It is evident from the plots that in the hard X-ray range, the model takes on a relatively flat and featureless shape. Our best fitting model reports a photon index of $\Gamma = 1.66^{+0.015}_{-0.015}$. This is similar to a spectral slope representative of the Seyfert population [Ricci et al., 2017]. However, this is in contrast to previous X-ray analyses of NGC 1052, reporting values in the range of 1.0 - 1.6 [Guainazzi and Antonelli, 1999, Osorio-Clavijo et al., 2019]. We also observe that the expected Compton hump, which typically peaks at ~ 30 keV, does not have a significant presence in our model.

In Table 3, we report the numerical values that untied parameters converge to in our three best-fitting models with 1σ errors. The three models are able to constrain some parameters relatively well in relation to each other. This is apparent with the plasma temperature parameter within the `mekal` component, where all three models agree (within their errors) to be 0.63 keV. This value agrees well with previous X-ray analysis of NGC 1052 [Brenneman et al., 2009, Osorio-Clavijo et al., 2019]. Additionally, all three models feature a first neutral absorber with a column density between 3.38-3.59 $(\times 10^{22}\ \mathrm{cm}^{-2})$ which absorbs $\sim 80\%$ of the incident spectrum, and a more dominant second absorber with a column density between 17.36-18.07 $(\times 10^{22}\ \mathrm{cm}^{-2})$ which absorbs $\sim 74\%$ of the spectrum. We can compare our resulting column densities with previous NGC 1052 analysis [Weaver et al., 1999] which reports a column density corresponding to our defined $N_{\mathrm{H},1}$ of $\sim$ 3-5 $(\times 10^{22}\ \mathrm{cm}^{-2})$ and a secondary column density corresponding to our $N_{\mathrm{H},2}$ of $\sim$ 3-5 $(\times 10^{23}\ \mathrm{cm}^{-2})$. Our value corresponding to $N_{\mathrm{H},1}$ agrees well with the previous analysis. However our model produces a slightly lower value for our more substantial absorber, $N_{\mathrm{H},2}$, which most likely represents the absorption due to the presence of the torus.

In Figure 9, we visualize the geometrical configuration of NGC 1052 as defined by our model. While Figure 1 displays the current accepted model for obscured AGN, our approach utilizes the `borus02` component which models the torus as a sphere of constant density with conical cutouts along the jet axis. We define the angle of orientation to be 76° following previous work, which is detailed in Section 1.2, orienting the approaching jet and jet axis to be closer to the line of sight of the observer. Furthermore, Model 3 reports an expected toroidal covering factor of $\sim 80\%$ allowing us to visualize a more dominant obscuring feature within our figure.

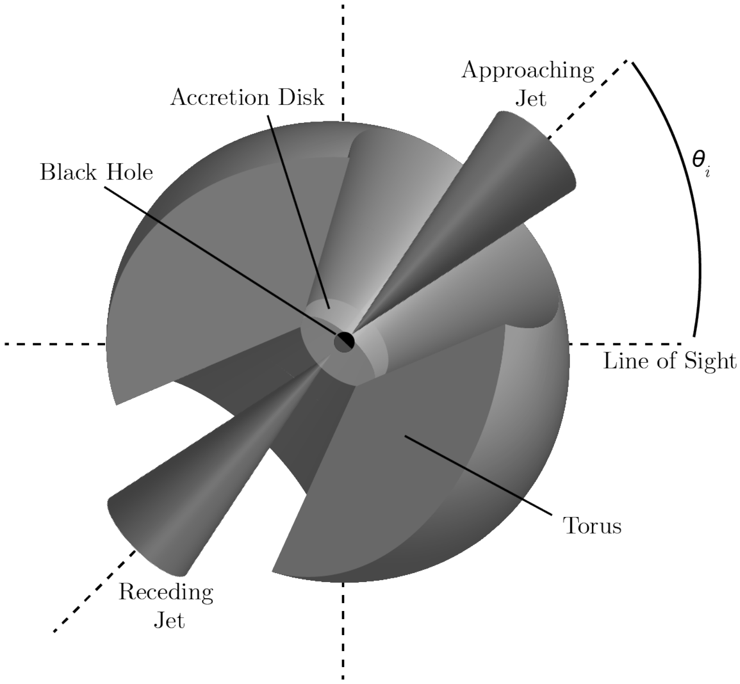

Figure 9: Our modeled configuration of NGC 1052. The expected geometrical definition of the torus is defined to be a uniformly dense sphere with conical cutouts. Model 3 reports a covering factor of $\sim 80\%$, allowing us to visualize the torus as being a more dominant feature than previously illustrated.

4.2 NGC 1052 Spectral Variability

Previous studies have shown that for AGN with relatively low accretion rates, an increase in luminosity corresponds to a decrease in the photon index that is characteristic of the emission spectrum. This notion is further explored by testing the spectral variability for 24 local AGN with low accretion rates [Connolly et al., 2016]. Their findings suggest that a ‘harder-when-brighter’ correlation is present within the data for NGC 1052, and that the photon index can be related to the flux with a simple linear function defined by Equation 4.1.

$$\Gamma = (-0.52\,\mathrm{ergs}^{-1}\,\mathrm{s})(\mathrm{Flux}) + 2.07 \tag{4.1}$$

We test this relation in application to our best-fitting model, which requires us to modify the defined photon index. We now allow the photon index to vary once per epoch. Corresponding luminosities are calculated with the `lumin` command in XSPEC and plotted for each epoch in Figure 10, where the average luminosity held by the *Swift*/BAT average is denoted by a black star. The linear equation defined in Equation 4.1 is adjusted to instead relate photon index to luminosity.

Our findings displayed in Figure 10 indicate that there is no clear relationship between photon index and luminosity within the confines of our model as previously expected for AGN with low accretion rates. However, this relationship should be further tested by applying our best-fitting model, which allows for time variation of important spectral features, to a large sample of AGN.

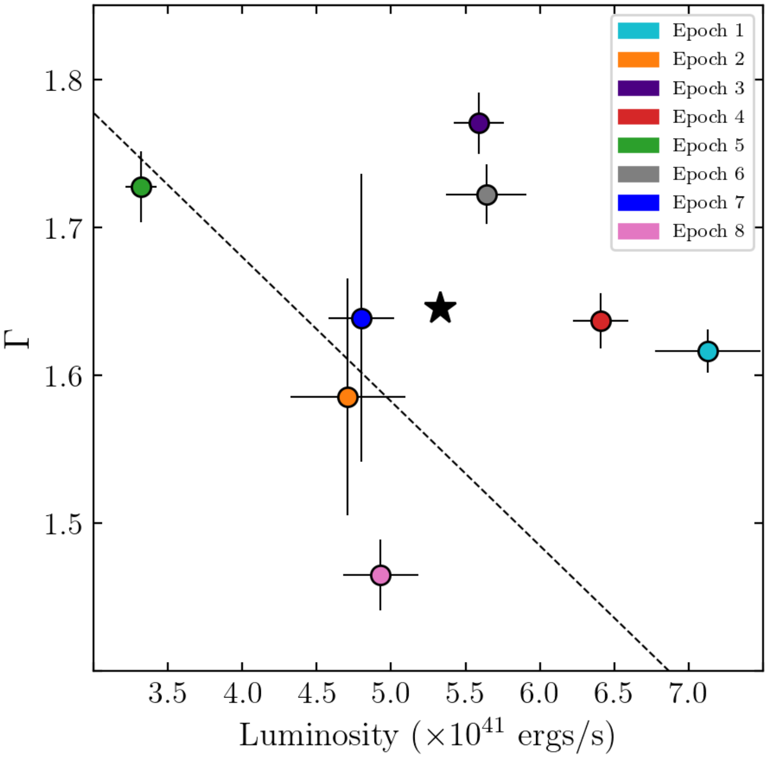

Figure 10: Spectral variability in NGC 1052. We test the "harder-when-brighter" relationship expected for low-luminosity AGN by plotting variation in luminosity as a function of photon index. The dotted line function represents the expected linear relationship defined in literature.

4.3 Post-Analysis Modeling Tests

Throughout the modeling process, we implement modifications to our model that test other possible initial conditions for our finalized version. While some of these modifications are complex and involve addition of new components that alter the model we defined in Section 3.1, the majority of the tests involve simple redefining of pre-existing parameters. The parameter changes that we explore throughout the modeling process, but could not contribute to a better-fitting model, are as follows.

1. Different assumption for the inclination angle. The inclination angle has not been well constrained previously, leading to minor discrepancies in the literature. While we adopted 80° inclination for our `borus02` spectral component, various studies have suggested that this angle could be as low as 50° [Kameno et al., 2001, Sawada-Satoh et al., 2008]. More recent work has suggested an angle as high as 86° [Baczko et al., 2016]. To test if a change in this angle would influence our spectral fit, we also considered an inclination angle of 60°, which corresponds to $cos(\theta_i) = 0.5$.

2. Freeing the high energy cutoff. When freeing the high-energy cutoff previously defined in our model as 300 keV, the parameter converges to a significantly lower value of $E_{\rm cut} = 119.7^{+74.1}_{-37.4}$ keV.

3. Freeing instrumental cross-normalization constants. Our finalized model utilizes cross-normalization constants listed in Table 2 to account for differences in flux calibrations among the various instrumentation we used. However, we also explore allowing these parameters to vary within the fit. Both *NuSTAR*/FPMA and *Swift*/BAT are still considered perfectly calibrated and their cross-normalization parameters remained at 1.0.

4. Freeing log $N_{\mathrm{H,tor}}$. Our finalized model defines the log of the torus column density to be equal to the log of the Compton scattering column density in `cabs`, though we test a model where this parameter is allowed to converge to a value not tied to the Compton scattering parameter. This results in the torus column density converging to a value of log $N_{\mathrm{H,tor}} = 23.101^{+0.031}_{-0.066}$ cm^{-2}.

We also explore methods of characterizing the AGN accretion disk. A previously common method of modeling is `pexrav` [Magdziarz and Zdziarski, 1995], which considers possible Compton reflection from a neutral accretion disk. We chose to model the neutral reflection with an updated version of this model, `pexmon` [Nandra et al., 2007], which expands on `pexrav` by considering absorption lines for Fe Kα, Fe Kβ, and Ni Kα. We include the model as an additive component to our original powerlaw and consider the same high energy cutoff value of 300 keV that was used previously. X-ray emissions are thought to originate from a source close to the accretion disk, so we make the assumption that both the intrinsic powerlaw and disk component vary in a similar manner. The disk normalization is then set to be equal to the varying power law normalization.

Additionally, we test including a scaling component, `kdblur` [Laor, 1991], to our disk reflection component. This allows for convolution of the `pexmon` component by considering the possible relativistic influence from a rotating black hole on the nearby accretion disk. The powerlaw dependence parameter is held at 3.0, the inner radius of emission from the disk (r_i) is set at 10.0 r_g, and the outer radius (r_o) is held at 400 r_g where $r_g = GM/c^2$.

While we tested considering the accretion disk at multiple stages throughout our modeling process, it did not improve the fit statistic. Introducing these modeling components to our best-fitting model produces a fit statistic of $\chi^2/\nu = 2045.13/1834$ (1.12).

Table 4: Supplementary observation information. These observations could not hold unique epochs due to low exposure times and low photon count rates. The *Chandra* and co-added *Swift* observations are compared to our best-fitting model in Section 4.4.

Observatory	OBSID or SID	Start Date	Epoch	Exposure (ks)	Instrument(s)
Swift	00030874001	2015 Jan. 19	-	9.34	XRT
Swift	00030874016	2009 June 29	-	1.11	XRT
Swift	00030874014	2009 June 26	-	9.71	XRT
Swift	00030874007	2008 Sep. 12	-	3.77	XRT
Swift	00030874006	2008 Sep. 9	-	4.74	XRT
Swift	00030874003	2007 Aug. 4	-	2.33	XRT
Chandra	385	2009 Aug. 29	-	2.34	ACIS

We can improve on this fit by leaving r_i and r_o as free parameters. However, this leads to values for these parameters that are not well constrained.

Lastly, we explore the possibility of absorption due to the presence of an ionized material. We accomplish this by defining the secondary absorption model component as `zxipcf`. While previous analysis of NGC 1052 have found success introducing ionized absorption into their model, we find that the resulting column density ($N_{\mathrm{H},2}$) converges to a value far less than expected. This indicates that any additional absorption of the spectrum is due to the presence of a neutral, not an ionized, medium.

4.4 Comparison to Additional Lower-quality Data

While we initially explored all of the available data, additional *Swift*/XRT and *Chandra* observations were utilized and held unique epochs. However, these observations were characterized by short exposure times and low photon count rates. This produced epochs with lower-quality data, leading to corresponding models that could not be correctly fitted and in general impaired our ability to produce a well-fitting model with our multi-epoch approach. The *Swift*/XRT and *Chandra* observations that were ultimately removed from our data set are listed below the double line in Table 1.

We again consider the previously removed data to explore its agreement with our finalized model. To accomplish this, we co-add the six *Swift*/XRT observations to produce one observation with higher data quality. We then plot this co-added observation and removed *Chandra* observation alongside the multi-epoch model comparison produced by the eight unique epochs from Model 3. This is displayed in Figure 11, where red denotes the *Swift*/XRT data and blue denotes the *Chandra* data.

We fit Model 3 without considering the newly added data, allowing us to visualize how these ”epochs” compare to our defined best-fitting model. While these observations hold the same general shape as the model, residuals are seen in the low-energy range. While the removed data lead to parameters that could not be well-constrained within the modeling process, it is evident that our best-fitting model will agree with all available X-ray observations of NGC 1052.

4.5 Torus Constraints Within the NGC 1052 Spectrum

We demonstrate the benefit of our multi-epoch approach by applying constraints in the parameter space spanned by the torus column density ($N_{\mathrm{H,tor}}$) and torus covering factor (C_{tor}) from the `borus02` model to three different singular epochs. Epoch 7 (*BeppoSAX*), Epoch 4 (*Suzaku*), and epoch 1 (joint *NuSTAR+XMM*) are chosen as the singular epochs to demonstrate the contours of 1, 2, and 3σ parameter constraints. These epochs are chosen for their strong coverage in both the soft and hard X-ray bands. We compare the constraints for the three singular epochs to the constraints for the multi-epoch data comprised of eight unique epochs in Figure 12.

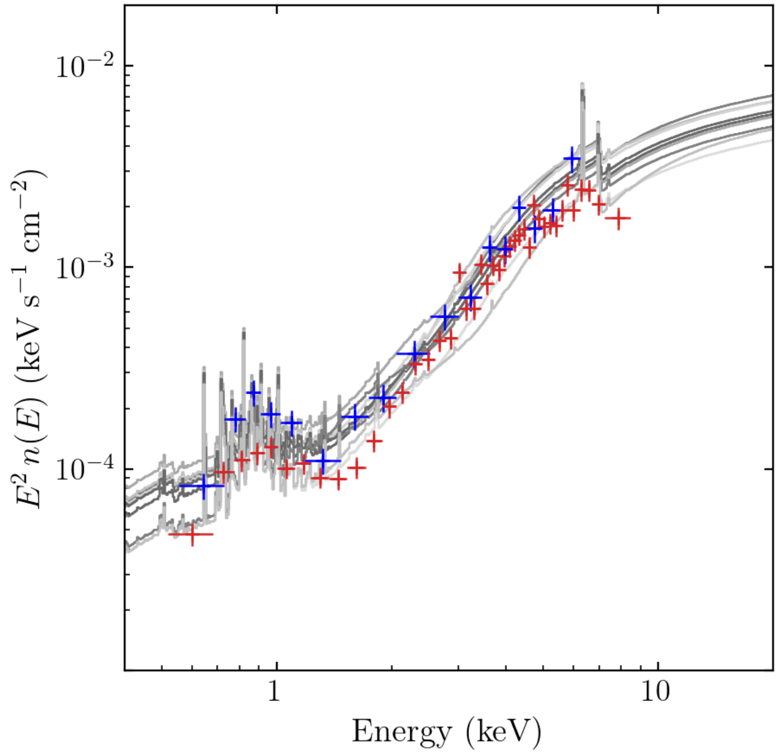

Figure 11: Model comparison to supplementary observations. We test the agreement between Model 3 to additional data not originally considered within the modeling process. Here, the blue spectrum represents an additional *Chandra* observation, while the red spectrum represents the co-added *Swift* observations.

This figure strongly suggests that the use of a large data set to employ time-varying parameters leads to a model that is significantly better constrained when compared to a singular epoch, even if the single epoch has exceptional data coverage.

4.6 Updated Tools for Torus Modeling

We introduce an extension to the `borus` set of models, `borus12` [Baloković et al., 2019], which serves as an update to the `borus02` component used throughout our modeling process. This updated table follows the same basic geometry as `borus02`, modeling the torus as a uniformly dense sphere with conical cutouts along the jet axis. The primary difference between models lies in the preferred representation of the intrinsic spectrum. Where we consider the intrinsic portion of our spectrum to best be represented as a powerlaw, `borus12` utilizes `nthcomp` [Zdziarski et al., 1996, Życki et al., 1999]. Therefore, to correctly update our model with the `borus12` component, we must also replace `cutoffpl` with `nthcomp` to update the continuum shape. This new component is defined by a black-body photon distribution with a temperature of 0.05 keV. We define the coronal electron photon temperature within `borus12` to be equal to kT_e/keV, the electron temperature divided by the plasma temperature, which serves as the high-energy cutoff we previously define as 300 keV in our powerlaw model.

This new approach to modeling the NGC 1052 spectrum fits relatively well, producing a fit statistic of $\chi^2/\nu = 2000.57/1758$ (1.14). Average line-of-sight column densities are calculated to be $\overline{N_{\mathrm{H},1}} = 4.14$ ($\times\,10^{22}$ cm^{-2}) and $\overline{N_{\mathrm{H},2}} = 29.14$ ($\times\,10^{22}$ cm^{-2}), suggesting a much stronger presence of spectral absorption due to the obscuring torus. A significant change emerges in the toroidal covering factor, with the inclusion of `borus12` suggesting a factor as low as $\sim 56\,\%$. This is a considerable decrease from the covering factor of 80 % produced by Model 3. However, it is important to note that choosing

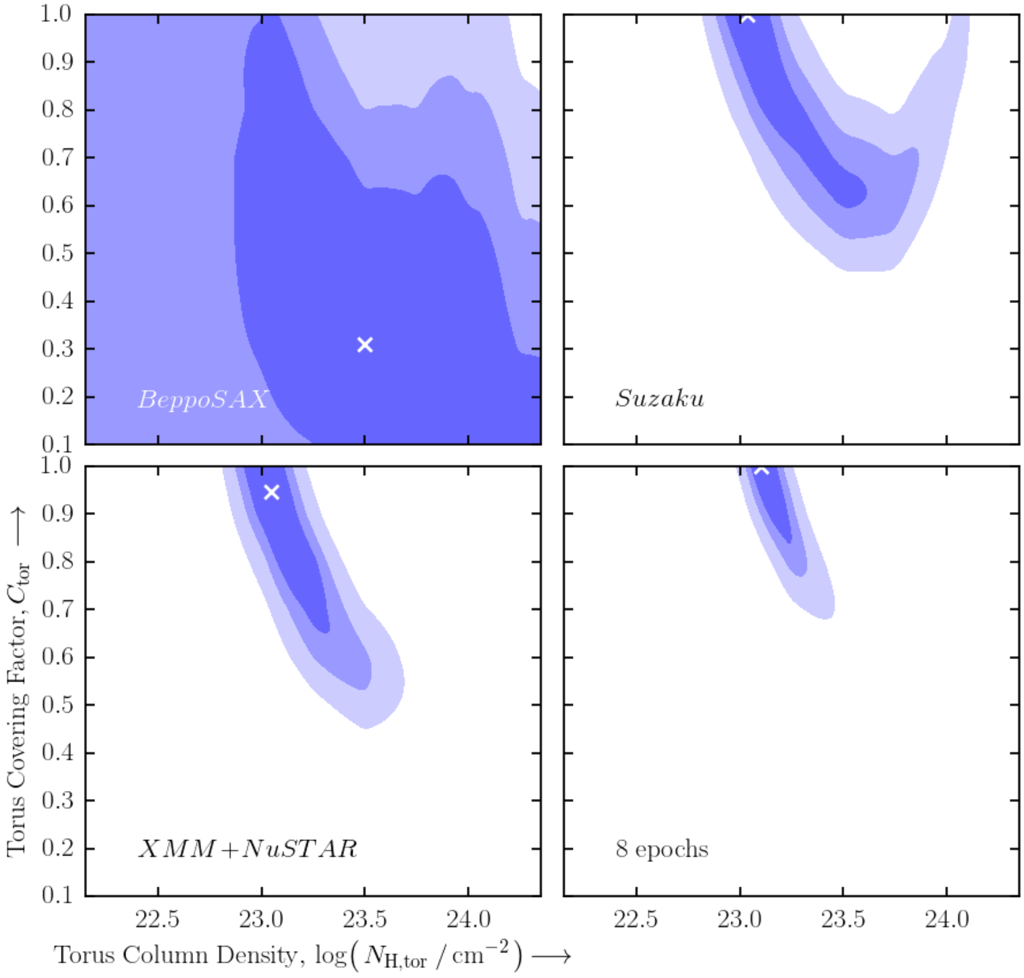

Figure 12: Contour plots comparing $N_{\rm H,tor}$ amd $C_{\rm tor}$. Constraints in the parameter space for the two parameters are plotted based on the `borus02` model applied to single-epoch and multi-epoch data. Contours show 1, 2, and 3σ constraints going from darkest to lightest colors. The first three panels show single epoch data for *BeppoSAX*, *Suzaku*, and joint *XMM* and *NuSTAR* observations taken in 2001, 2007, and 2017, respectively. The rightmost panel displays constraints from the joint modeling of eight epochs.

.

specific components to utilize when modeling our spectra in addition to any underlying assumptions that are made when using modeling components may have significant impact on constraints of parameters. This introduces a factor of uncertainty that should be quantified in any future analysis.

CHAPTER 5

CONCLUSION

Our multi-epoch approach to modeling the X-ray spectrum of NGC 1052 and utilization of years of data proved useful in demonstrating the long-term variability of a heavily obscured AGN's spectrum. Organizing observations by date into distinct epochs allowed us to create a model that was sensitive to possible spectral variations that may have occured over time. As previously mentioned, this allows us to better constrain the obscuring nature of NGC 1052 by quantifying specific parameters such as the neutral absorption column densities and covering fraction.

Our model suggests that the spectrum of NGC 1052 can best be explained with the presence of two neutral absorption components, where the more dominant of the two represents obscuration from the torus, while the second component represents galactic absorption from the AGN's host galaxy. While these parameters were allowed to vary throughout the model, we observe average line-of-sight column densities from Model 3 to be $\overline{N_{\mathrm{H},1}} = 3.38 \times 10^{22}\ \mathrm{cm}^{-2}$ and $\overline{N_{\mathrm{H},2}} = 18.07 \times 10^{22}\ \mathrm{cm}^{-2}$.

Our approach allows us to effectively constrain properties of the torus. Our analysis suggests that the torus of NGC 1052 features a dominant covering factor of $\sim$80%, with an average line-of-sight column density of $\log N_{\mathrm{H,tor}} = 23.10\ \mathrm{cm}^{-2}$. By visualizing constraints in the parameter space of the torus column density versus the covering factor in Figure 12, we demonstrate that our multi-epoch approach with a varying model is significantly more beneficial than only utilizing singular epochs, regardless of how much energy coverage those singular epochs provide.

Acknowledgment

The authors gratefully acknowledge support from the Black Hole Initiative at Harvard University, funded through a grant from the John Templeton Foundation. This research has made use of data and/or software provided by the High Energy Astrophysics Science Archive Research Center (HEASARC), which is a service of the Astrophysics Science Division at NASA/GSFC. Based on observations obtained with XMM-Newton, an ESA science mission with instruments and contributions directly funded by ESA Member States and NASA. This research has made use of data obtained from the Chandra Data Archive and the Chandra Source Catalog, and software provided by the Chandra X-ray Center (CXC) in the application packages CIAO, ChIPS, and Sherpa. This research has made use of the Tartarus (Version 3.1) database, created by Paul O'Neill and Kirpal Nandra at Imperial College London, and Jane Turner at NASA/GSFC. Tartarus is supported by funding from PPARC, and NASA grants NAG5-7385 and NAG5-7067.

REFERENCE LIST

[Antonucci, 1993] Antonucci, R. (1993). Unified Models for Active Galactic Nuclei and Quasars. *Annual Rev. Astron. Astrophys.*, 31:473–521.

[Baczko et al., 2016] Baczko, A. K. et al. (2016). A Highly Magnetized Twin-jet Base Pinpoints a Supermassive Black Hole. *Astronomy and Astrophysics*, 593:A47.

[Baloković et al., 2018] Baloković, M. et al. (2018). New Spectral Model for Constraining Torus Covering Factors from Broadband X-Ray Spectra of Active Galactic Nuclei. *The Astrophysical Journal*, 854(1):42.

[Baloković et al., 2019] Baloković, M., García, J. A., and Cabral, S. E. (2019). New Tools for Self-consistent Modeling of the AGN Torus and Corona. *Research Notes of the American Astronomical Society*, 3(11):173.

[Boella et al., 1997a] Boella, G. et al. (1997a). BeppoSAX, the Wide Band Mission for X-ray Astronomy. *Astron. Astrophys. Suppl. Ser.*, 122:299–307.

[Boella et al., 1997b] Boella, G. et al. (1997b). The Medium-energy Concentrator Spectrometer on Board the BeppoSAX X-ray Astronomy Satellite. *Astron. Astrophys. Suppl. Ser.*, 122:327–340.

[Brenneman et al., 2009] Brenneman, L. W. et al. (2009). Spectral Analysis of the Accretion Flow in NGC 1052 with Suzaku. *The Astrophysical Journal*, 698(1):528–540.

[Brightman and Nandra, 2011] Brightman, M. and Nandra, K. (2011). An XMM-Newton Spectral Survey of 12 μm Selected Galaxies - I. X-ray Data. *Monthly Notices of the Royal Astronomical Society*, 413(2):1206–1235.

[Connolly et al., 2016] Connolly, S. D., McHardy, I. M., Skipper, C. J., and Emmanoulopoulos, D. (2016). Long-term X-ray spectral variability in AGN from the Palomar sample observed by Swift. *Monthly Notices of the Royal Astronomical Society*, 459(4):3963–3985.

[Frontera et al., 1997] Frontera, F. et al. (1997). The High Energy Instrument PDS Onboard the BeppoSAX X–ray Astronomy Satellite. *Astron. Astrophys. Suppl. Ser.*, 122:357–369.

[Gabriel et al., 2004] Gabriel, C. et al. (2004). The XMM-Newton SAS - Distributed Development and Maintenance of a Large Science Analysis System: A Critical Analysis. In Ochsenbein, F., Allen, M. G., and Egret, D., editors, *Astronomical Data Analysis Software and Systems (ADASS) XIII*, volume 314 of *Astronomical Society of the Pacific Conference Series*, page 759.

[Gehrels and Swift Team, 2003] Gehrels, N. and Swift Team (2003). The Swift Gamma Ray Burst Mission. In *American Astronomical Society Meeting Abstracts*, volume 203, page 62.06.

[George and Fabian, 1991] George, I. M. and Fabian, A. C. (1991). X-ray Reflection from Cold Matter in Active Galactic Nuclei and X-ray binaries. *Monthly Notices of the Royal Astronomical Society*, 249:352.

[Guainazzi and Antonelli, 1999] Guainazzi, M. and Antonelli, L. A. (1999). The Flat X-ray Spectrum of the LINER NGC 1052. *Monthly Notices of the Royal Astronomical Society*, 304(1):L15–L19.

[Haardt and Maraschi, 1991] Haardt, F. and Maraschi, L. (1991). A Two-phase Model for the X-ray Emission from Seyfert galaxies. *Astrophysical Journal Letters*, 380:L51–L54.

[Harrison et al., 2013] Harrison, F. A. et al. (2013). The Nuclear Spectroscopic Telescope Array (NuSTAR) High-energy X-Ray Mission. *The Astrophysical Journal*, 770:103.

[HI4PI Collaboration et al., 2016] HI4PI Collaboration et al. (2016). HI4PI: A Full-sky H I Survey Based on EBHIS and GASS. *Astronomy and Astrophysics*, 594:A116.

[Inoue, 1993] Inoue, H. (1993). The X-ray Astronomy Satellite “ASCA”. *Experimental Astronomy*, 4(1):1–10.

[Jansen et al., 2001] Jansen, F. et al. (2001). XMM-Newton Observatory. I. The Spacecraft and Operations. *Astronomy and Astrophysics*, 365:L1–L6.

[Jensen et al., 2003] Jensen, J. B. et al. (2003). Measuring Distances and Probing the Unresolved Stellar Populations of Galaxies Using Infrared Surface Brightness Fluctuations. *The Astrophysical Journal*, 583(2):712–726.

[Kadler et al., 2004] Kadler, M. et al. (2004). Jet Emission in NGC 1052 at Radio, Optical, and X-ray Frequencies. *Astronomy and Astrophysics*, 420:467–474.

[Kameno et al., 2001] Kameno, S. et al. (2001). The Dense Plasma Torus Around the Nucleus of an Active Galaxy NGC1052. *Publications of the Astronomical Society of Japan*, 53(2):169–178.

[Koyama et al., 2007] Koyama, K. et al. (2007). X-Ray Imaging Spectrometer (XIS) on Board Suzaku. *Publications of the Astronomical Society of Japan*, 59:23–33.

[Krimm et al., 2013] Krimm, H. A. et al. (2013). The Swift/BAT Hard X-Ray Transient Monitor. *The Astrophysical Journal Supplement*, 209(1):14.

[Krolik et al., 1994] Krolik, J. H., Madau, P., and Zycki, P. T. (1994). X-ray Bumps, Iron K-alpha Lines, and X-ray Suppression by Obscuring Tori in Seyfert galaxies. *Astrophysical Journal Letters*, 420:L57–L61.

[Laor, 1991] Laor, A. (1991). Line Profiles from a Disk around a Rotating Black Hole. *The Astrophysical Journal*, 376:90.

[Levenson et al., 2002] Levenson, N. A., Krolik, J. H., Życki, P. T., Heckman, T. M., Weaver, K. A., Awaki, H., and Terashima, Y. (2002). Extreme X-Ray Iron Lines in Active Galactic Nuclei. *The Astrophysical Journal*, 573:L81–L84.

[Madsen et al., 2017] Madsen, K. K. et al. (2017). IACHEC Cross-calibration of Chandra, NuSTAR, Swift, Suzaku, XMM-Newton with 3C 273 and PKS 2155-304. *The Astronomical Journal*, 153(1):2.

[Magdziarz and Zdziarski, 1995] Magdziarz, P. and Zdziarski, A. A. (1995). Angle-dependent Compton Reflection of X-rays and Gamma-rays. *Monthly Notices of the Royal Astronomical Society*, 273(3):837–848.

[Markowitz et al., 2014] Markowitz, A. G., Krumpe, M., and Nikutta, R. (2014). First X-ray-based Statistical Tests for Clumpy-torus Models: Eclipse Events from 230 years of Monitoring of Seyfert AGN. *Monthly Notices of the Royal Astronomical Society*, 439:1403–1458.

[Mewe et al., 1985] Mewe, R., Gronenschild, E. H. B. M., and van den Oord, G. H. J. (1985). Calculated X-radiation from Optically Thin Plasmas. V. *Astronomy and Astrophysics, Suppl. Ser.*, 62:197–254.

[Mitsuda et al., 2007] Mitsuda, K. et al. (2007). The X-Ray Observatory Suzaku. *Publications of the Astronomical Society of Japan*, 59:S1–S7.

[Murphy and Yaqoob, 2009] Murphy, K. D. and Yaqoob, T. (2009). An X-ray Spectral Model for Compton-thick Toroidal Reprocessors. *Monthly Notices of the Royal Astronomical Society*, 397(3):1549–1562.

[Nandra et al., 2007] Nandra, K. et al. (2007). An XMM-Newton Survey of Broad Iron Lines in Seyfert Galaxies. *Monthly Notices of the Royal Astronomical Society*, 382(1):194–228.

[Oh et al., 2018] Oh, K. et al. (2018). The 105-Month Swift-BAT All-sky Hard X-Ray Survey. *The Astrophysical Journal Supplement Series*, 235:4.

[Ohashi et al., 1996] Ohashi, T. et al. (1996). The Gas Imaging Spectrometer on Board ASCA. *Publications of the Astronomical Society of Japan*, 48:157–170.

[Osorio-Clavijo et al., 2019] Osorio-Clavijo, N. et al. (2019). The Inner View of NGC 1052 Using Multiple X-ray Observations. *arXiv e-prints*, page arXiv:1910.01660.

[Parmar et al., 1997] Parmar, A. N. et al. (1997). The Low-energy Concentrator Spectrometer On-board the BeppoSAX X-ray Astronomy Satellite. *Astron. Astrophys. Suppl. Ser.*, 122:309–326.

[Ricci et al., 2017] Ricci, C. et al. (2017). BAT AGN Spectroscopic Survey. V. X-Ray Properties of the Swift/BAT 70-month AGN Catalog. *The Astrophysical Journal Supplement Series*, 233(2):17.

[Risaliti et al., 2002] Risaliti, G., Elvis, M., and Nicastro, F. (2002). Ubiquitous Variability of X-Ray-absorbing Column Densities in Seyfert 2 Galaxies. *The Astrophysical Journal*, 571(1):234–246.

[Sawada-Satoh et al., 2008] Sawada-Satoh, S. et al. (2008). Positional Coincidence of H_2O Maser and a Plasma-Obscuring Torus in Radio Galaxy NGC 1052. *The Astrophysical Journal*, 680(1):191–199.

[Shakura and Sunyaev, 1973] Shakura, N. I. and Sunyaev, R. A. (1973). Black Holes in Binary systems. Observational appearance. *Astronomy and Astrophysics*, 500:33–51.

[Snowden, 2002] Snowden, S. L. (2002). Comparison of XMM-Newton EPIC, Chandra ACIS-S3, ASCA SIS and GIS, and ROSAT PSPC Results for G21.5-0.9, 1E0102.2-7219, and MS1-54.4-0321. *arXiv e-prints*, pages astro–ph/0203311.

[Takahashi et al., 2007] Takahashi, T. et al. (2007). Hard X-Ray Detector (HXD) on Board Suzaku. *Publications of the Astronomical Society of Japan*, 59:35–51.

[Tanaka et al., 1994] Tanaka, Y., Inoue, H., and Holt, S. S. (1994). The X-Ray Astronomy Satellite ASCA. *Publications of the Astronomical Society of Japan*, 46:L37–L41.

[Urry and Padovani, 1995] Urry, C. M. and Padovani, P. (1995). Unified Schemes for Radio-Loud Active Galactic Nuclei. *Publications of the Astronomical Society of the Pacific*, 107:803.

[Weaver et al., 1999] Weaver, K. A. et al. (1999). X-Ray Emission from the Prototypical LINER Galaxy NGC 1052. *The Astrophysical Journal*, 520(1):130–136.

[Weisskopf et al., 2002] Weisskopf, M. C. et al. (2002). An Overview of the Performance and Scientific Results from the Chandra X-Ray Observatory. *Publications of the Astronomical Society of the Pacific*, 114(791):1–24.

[Zdziarski et al., 1996] Zdziarski, A. A., Johnson, W. N., and Magdziarz, P. (1996). Broad-band γ-ray and X-ray Spectra of NGC 4151 and Their Implications for Physical Processes and Geometry. *Montly Notices of the Royal Astronomical Society*, 283(1):193–206.

[Życki et al., 1999] Życki, P. T., Done, C., and Smith, D. A. (1999). The 1989 May Outburst of the Soft X-ray Transient GS 2023+338 (V404 Cyg). *Monthly Notices of the Royal Astronomical Society*, 309(3):561–575.